PHYSICAL REVIEW B **75**, 094113 (2007)

Multistate modified embedded atom method

M. I. Baskes,* S. G. Srinivasan, S. M. Valone, and R. G. Hoagland
Materials Science Division, Los Alamos National Laboratory, Los Alamos, New Mexico 87545, USA

(Received 6 July 2006; revised manuscript received 6 October 2006; published 27 March 2007)

A multireference state formalism for determining the functions for the modified embedded atom method (MEAM) is developed. This formalism eliminates almost all of the prior arbitrary choices in the MEAM function determination and replaces it with first-principles calculations of the MEAM electron densities, embedding energy, pair potential, and angular screening functions. The formalism accepts any level of first-principles information and is applicable to all elements. It may be considered as a physically based interpolation of the first-principles data for systems that fall within the range covered by that data. The critical addition of multiple reference states includes the energy/volume relationship for those reference structures as well as reference paths connecting the reference structures. The formalism is applied to Cu as a model material. Extensive predictions of the model are made and compared to additional first-principles calculations, results of two literature EAM potentials, and experiment. Our model, which uses as input only the first-principles database, represents the first-principles calculations extremely well (better than the EAM calculations). Furthermore, it agrees with experiments almost as well as EAM models, derived from a combination of first-principles calculations and experiments.

DOI: 10.1103/PhysRevB.75.094113 PACS number(s): 64.10.+h, 64.30.+t, 65.40.−b, 68.18.Fg

I. INTRODUCTION

High fidelity atomistic simulations are predicated upon the availability of a computationally efficient and accurate description of interatomic interactions. Over two decades ago Daw and Baskes[1,2] introduced the embedded atom method (EAM) as a superior alternative to central-body pair potential interactions. Since then, EAM and EAM-like methods such as the glue model[3] and *N*-body potentials[4] have become the mainstay of semi-empirical atomistic calculations. Although predictions using these methods have generally been quite good, both qualitatively and quantitatively superior to the early pair potential calculations, unfortunately these methods suffer from a major deficiency in that the theory leads to non-unique potential functions. The literature is now replete with EAM-type functions, each predicting slightly different material properties and often yielding only qualitative results. Therefore, for computational materials science to become a predictive method of materials selection, we need to develop more reliable interatomic potentials.

The purpose of a semi-empirical atomistic model is to predict the bond energy between two atoms. Four critical factors enter into the calculation of the bond energy. The most important factor is the bond distance. This factor was captured by early pair interaction models. Second in importance is the local coordination. This concept is embodied in the EAM. Third is the variation in bond energy with highly symmetric local arrangement of atoms. The critical effect here is the angular dependence of the electron density, which manifests itself in directional bonding and bond-bending forces. The modified EAM (MEAM) was developed to model this effect.[5–7] Finally, the bond energy depends on local defects or large strains. Transformation paths that change the local coordination capture this behavior. These four themes, bond length, coordination, symmetric local arrangement, and transformations and deformations will be more fully developed below.

Central to the EAM is the connection to a reference structure. Traditional models previous to the inception of the EAM typically used equilibrium properties to determine the model parameters, e.g., lattice constant and cohesive energy as used in the Lennard-Jones model.[8] In the EAM, the reference structure was chosen to extend these properties to nonequilibrium conditions. Specifically the energy/volume relationship for a specific crystal structure (usually the ground state) was reproduced exactly by construction. At this time the so-called universal equation of state (UEOS) (Ref. 9) had been developed. The UEOS was a simple way to obtain the energy/volume relationship using the experimental equilibrium lattice constant, cohesive energy, and bulk modulus. The use of the UEOS facilitates the correct bond energy–bond length relationship for the chosen reference state.

Over this same period of time, increasing computing power and development of different algorithms have permitted first-principles calculations to evolve into a tractable and reasonably accurate method for determining the energetics of various simple atomic configurations. The accuracy of first-principles calculations is approaching that needed for the prediction of chemical reactivity and material properties. Unfortunately, due to the large computational cost of these calculations, properties other than very simple ones are inaccessible. For example, the 0 K lattice constants and elastic constants for high-symmetry crystal structures can be readily calculated using first-principles methods, but it is usually not possible to calculate directly their temperature dependence or the free energies of different phases. Only by using additional, less accurate, models are such quantities routinely calculated.

Nevertheless, the accuracy of first-principles calculations for these high-symmetry systems now opens up an opportunity in the area of semi-empirical potentials. We now can use not only the energy/volume relationship derived from experiment for crystal structures that occur in nature, but also the energy/volume relationships for other crystal structures that do not exist in nature. The use of energy/volume relationships for structures of different coordination and local environment allows us to capture the second and third themes discussed above. The use of multiple reference structures to develop EAM functions was used by Laskowski.[10]

Of course, complicated thermodynamic properties, such as those mentioned above, are readily calculated using semi-empirical or empirical potentials, but the energetics of these potentials for structures away from the reference structure are not as accurate as the first-principles calculations. Thus, we now have a Morton's Fork, to use a first-principles method to determine an accurate energy and a simple model to obtain a questionable entropy, or employ a semi-empirical potential to determine a questionable energy and more accurate entropy. The present paper circumvents this dilemma by describing an approach to develop a family of high fidelity, computationally inexpensive, semi-empirical potentials that are essentially an interpolation among multiple reference states, as opposed to an extrapolation from a single reference state, of first-principles calculations. We propose that quantitative thermodynamic properties of materials may be calculated relatively easily using our method.

As an example of this method, in this work, we choose Cu as a model material, and use a standard first-principles method (VASP), within the framework of density functional theory (DFT), to calculate a reference database. We derive our semi-empirical potential using this reference database. The database not only includes the energetics of a number of reference structures as discussed above, but also energetics of the transformation paths between these structures. We call these transformation paths, reference paths. A reference state is either a reference structure or a reference path. By using reference structures, we capture the dependence of the bond energy on local coordination and atomic arrangement. Similarly, by using the reference paths, we capture the dependence of bond energy on large strain and changes in coordination.

Cu was chosen for three reasons: (i) the VASP calculations are straightforward compared to, e.g., more interesting materials that are magnetic; (ii) many EAM potentials are available for easy comparison; and (iii) this was a "worst case" for MS-MEAM with respect to improvement over EAM, i.e., any other material should show better improvement.

The method we develop is generally applicable to any (single component) material and any first-principles computational scheme and in no way is specific to Cu or VASP. We have found that it is necessary to include angular forces in our semi-empirical model to accurately represent the first-principles data; hence, we base our model on the modified EAM (MEAM).[5–7] For this reason, we name our model multistate MEAM, or MS-MEAM, to differentiate it from earlier approaches. In the next section, we describe the MEAM model, our first-principles method, and a simple analytic EAM model that shows how dual reference states may be implemented. We follow this with a section describing how the MEAM functions are determined from the first-principles database. Next, we conduct rigorous tests to determine the predictability and transferability of our MS-MEAM model. In this section, we also compare MS-MEAM to two EAM potentials, an old EAM potential by Foiles *et al.* (FBD),[11] and a modern EAM potential by Mishin *et al.* (MMPVK),[12] EAM1 also fit to first-principles data. Note that MMPVK was fit to first-principles linear augmented plane wave calculations, which in principle are more accurate than VASP, or at least give slightly different numbers that might account for some of the discrepancies between MS-MEAM and MMPVK. We conclude with a short summary.

II. THEORY

A. MEAM

Daw[13] has shown that the functional form of the EAM for a single component material follows directly from density functional theory. The form for the energy of an ensemble of atoms, E, is given by

$$E = \sum_i \left\{ F(\bar{\rho}_i) + \frac{1}{2}\sum_{j\neq i} \phi(R_{ij}) \right\}, \tag{1}$$

where F is the embedding energy for a background electron density $\bar{\rho}$, the pair potential ϕ is evaluated at the interatomic distance R_{ij}, and the sums are over atoms i and j. In order to have a computationally efficient method of calculation, i.e., order N where N is the total number of atoms, the pair potential is traditionally truncated at a specific distance (radial cutoff) or by the local environment of the neighbors of an atom (angular cutoff).[14] Previous work[15] has shown that the assumption of short ranged interactions in close-packed metals is a good one. In this work, we will use angular screening. Thus, the basic EAM ansatz becomes

$$E = \sum_i \left\{ F(\bar{\rho}_i) + \frac{1}{2}\sum_{j\neq i} \phi(R_{ij}) S_{ij}^{\phi} \right\}, \tag{2}$$

where we make the simple physical assumption that the net screening S_{ij}^{ϕ} is a multiplicative process mediated by neighboring atoms m:

$$S_{ij}^{\phi} = \prod_{m\neq i,j} S_{imj}^{\phi}, \tag{3}$$

and S_{imj}^{ϕ} is the screening function for the pair potential between atoms i and j by neighbors m.

We now expand the angular dependence of the background electron density as a series of partial electron densities, which depend on zero order Legendre polynomials, P_0^l:

$$\bar{\rho}_i^2 = (\rho_i^0)^2 + \sum_{l=1}^{3} [(\rho_i^{l+})^2 - (\rho_i^{l-})^2], \tag{4}$$

where, as in the EAM, the spherically symmetric electron density at atom i is given by

$$\rho_i^0 = \sum_{j\neq i} \rho^{a0}(R_{ij}) S_{ij}^{\rho^0}. \tag{5}$$

In EAM, the screening is usually implemented through a radial cut-off function. The partial electron densities at atom i are given by

$$(\rho_i^{l\pm})^2 = \sum_{j,k} P_0^l[\cos(\theta_{jik})]\rho^{al\pm}(R_{ij})\rho^{al\pm}(R_{ik})S_{ij}^{\rho^l}S_{ik}^{\rho^l}, \quad (6)$$

and as for ϕ, the screening for the atomic electron densities ρ^{al} is given by

$$S_{ij}^{\rho^l} = \prod_{m\neq i,j} S_{imj}^{\rho^l}. \quad (7)$$

The physical justification for Eqs. (4)–(6) is given in Appendix A. Note that in previous versions of MEAM a weighting factor t_l was used for the angularly dependent partial electron densities. Here this factor is absorbed into the partial electron densities. Additionally, to encompass both positive and negative changes to the background electron density, two partial electron densities ($\pm$) are included.

The complete MEAM is given by Eqs. (2)–(7). There are 14 unknown functions: $F, \phi, S_{imj}^{\phi}, \rho^{a0}, \rho^{al\pm}, l=1,3$, and $S_{imj}^{\rho^l}, l=0,3$, that will be determined below. In contrast, MMPVK and FBD EAM potentials have 28 and 7 free parameters, respectively. Note that all prior versions of MEAM have assumed that all of the angular screening functions were identical and that only either the positive or negative partial electron density was nonzero for each l. We find that the first-principles database requires the additional flexibility in the model presented above.

B. First-principles database: VASP

We calculate total energies using carefully converged *ab initio* VASP (Vienna *ab initio* simulation package) simulations.[16] VASP is a density functional theory (DFT) code using pseudopotentials (details below) and a plane-wave basis set. VASP calculates the Kohn-Sham ground state via an iterative unconstrained matrix diagonalization scheme and an efficient Pulay/Broyden charge density mixing. Sampling of the irreducible wedge of the Brillouin zone is performed with a regular Monkhorst-Pack grid of special points. Ground-state atomic geometries are obtained by minimizing the Hellman-Feyman forces using either a conjugate gradient or quasi-Newton algorithm, until the total force on each ion reaches convergence. The generalized gradient approximation (GGA) of Perdew and Wang is used for evaluating the exchange-correlation energy.[17]

A projector-augmented wave (PAW) method based Cu potential is used for all VASP calculations reported in this paper[18,19] as it yields better results for bulk properties of Cu. PAW pseudopotentials are generated with an atomic valence configuration of $(3d)^{10}(4s)^1$, which is the ground state as predicted by DFT. We first carry out plane-wave cutoff, k-point convergence tests, and Murnaghan equation fitting for bulk Cu to determine their optimum settings. A plane-wave kinetic-energy cutoff of 400 eV ensures energy convergence to 0.3 meV/atom, and a Monkhorst-Pack k-point mesh of $20\times20\times20$ guarantee an accuracy of 1 meV/atom in total energy calculations.

For each reference structure, the VASP energies are calculated at a number of discrete nearest neighbor distances (volumes) and specific points along the transformation paths between reference structures. More specifically, the ratio of the first nearest neighbor distance (r_{1NN}) to the equilibrium nearest neighbor distance of fcc Cu (r_0) varies from 0.7 to 4.0. We vary this by 0.1 for $r_{1NN}/r_0=0.7-2.0$ and by 0.2 for $r_{1NN}/r_0=2.0-4.0$. We calculate energies at 10–20 evenly spaced points along each transformation path. In order to have a continuum of energies for the MEAM function development, VASP fcc energy, and for other structures, VASP energy differences per bond, are fit to a series of exponentials. We wish to point out that although we calculate energies of the unrelaxed hcp structure with ideal c/a ratio, this does not pose a problem for modeling real hcp systems. If the model works accurately, the real hcp system should relax to its appropriate c/a ratio. Similarly, although we use Bain path information at only one bcc volume, the potential is able to predict correct energy versus volume as given by VASP.

In general, first-principles calculations of equilibrium lattice constant and cohesive energy do not exactly agree with experiment. To have a more flexible model, we scale all of the VASP energies so that the minimum energy of the fcc structure is -1 and scale all distances so that the nearest neighbor distance of this structure is 1. In this work, we will make most comparisons in this scaled system.

C. Analytical, two reference state illustration

Before we tackle the full multistate MEAM, we examine a very simple illustration of how two reference structures can be used to determine the MEAM functions. If one has knowledge of binding curves for two or more crystal structures of an element, then it is possible to place consistency requirements on the embedding function and/or background densities. The question of how to make the embedding functions consistent with two reference states has been addressed within the context of EAM.[10] It is known that the procedure is either unstable or at best poorly convergent.

Here we assume that the embedding energy functional form is known and we require consistency between the background densities for the two reference states where only nearest neighbor interactions are relevant. Suppose that we have reference monatomic crystal states a and b characterized as having Z_a and Z_b nearest neighbors and E_a^{ref} and E_b^{ref} binding curves, respectively.

From Eq. (2),

$$E_\lambda^{ref}(R) = F[(\bar{\rho}_\lambda(R)\ ] + \frac{Z_\lambda}{2}\phi(R), \quad \lambda = a,b, \quad (8)$$

where $\bar{\rho}_a$ and $\bar{\rho}_b$ are the background densities associated with the reference states. In the absence of angular forces (EAM):

$$\bar{\rho}_\lambda(R) = Z_\lambda \rho^{a0}(R), \quad \lambda = a,b, \quad (9)$$

where $\bar{\rho}_\lambda(R)$ is the atomic electron density. If we assume that the embedding function is given by the specific form

$$F = A\bar{\rho}\ln(\bar{\rho}), \quad (10)$$

by appropriate manipulation of Eq. (8):

$$\frac{E_a^{ref}(R)}{Z_a} - \frac{E_b^{ref}(R)}{Z_b} = A\rho^{a0}(R)\ln\left(\frac{Z_a}{Z_b}\right), \tag{11}$$

which is readily solved for $\rho^{a0}(R)$ using the known reference structure energies $E_\lambda^{ref}(R)$. Since we now know the atomic electron density, it is easy to determine ϕ using Eq. (8).

The fact that energies determine background densities is directly attributable to the DFT underpinnings of the model. This form of $\rho^{a0}(R)$ clearly entails participation of two reference states that enables the model to switch between configurations. Each of those reference states has its own functional dependence on R. As such, there is no requirement that $\rho^{a0}(R)$ be positive. (The present form of the embedding energy is undefined at those points.) Note that, in prior models of $\rho^{a0}(R)$, a single exponential decay was allowed. This illustration analytically displays the kind of physical behavior that we are trying to capture with a multiple-reference state determination of the MEAM model. A model of this form was used to formulate a united-atom model of polyethylene and to simulate shock compression of an amorphous polymer.[20,21]

To complete the MEAM model, the angular dependencies of $\bar{\rho}(R)$ and the screening functions are required. Below we present a method to determine these from additional reference states.

III. DETERMINATION OF MEAM FUNCTIONS

Previously for both EAM and MEAM, we have built the models around a single reference structure. That is, the energy of one crystal structure as a function of homogeneous deformation (lattice constant), usually the equilibrium ground state, is used to determine one of the unknown functions. Using this concept, the embedding function is usually determined for EAM and the pair potential is determined for MEAM. In this section, this concept is formally expanded, using multiple reference states, hence the name multistate MEAM or MS-MEAM. To aid the reader through this procedure, a summary of the reference states used and the corresponding MEAM function determined by that reference state is included in Table I.

A. Reference structures

1. Structures with only 1NN

The extraction of the functions in Eqs. (2)–(7) is simplified if we first examine only fcc, simple cubic (SC), hcp, diamond cubic (DC), a one-dimensional (1D) line, and a diatomic molecule (dimer) structures, where we may safely assume that interactions are determined by only the Z_1 first nearest neighbors (1NN). These structures have been chosen so that any atom in each structure has the same atomic environment; hence, every atom is equivalent and has the same atomic energy. In these structures, all 1NN have $S_{imj}=1$ and for more distant neighbors all $S_{imj}=0$ for both ϕ and ρ. For these simple cases the atomic energy is given by:

$$E = F(\bar{\rho}) + \frac{Z_1}{2}\phi(R) \tag{12}$$

TABLE I. Correspondence between the reference states and the MEAM function determined by that state. States and functions are defined in the text. The transformation paths are used in combination to determine the angular screening.

Reference state	Structure	Path	MEAM function
SC/fcc	X		$F(\bar{\rho})$
fcc	X		$\phi(R)$
line	X		$\Upsilon^2(R)$
hcp	X		$\Upsilon^3(R)$
dimer	X		$\Upsilon^1(R)$
DC	X		$\rho^{a0}(R)$
Bain		X	$S_{imj}^{\phi}(C)$
trigonal		X	$S_{imj}^{\rho 0}(C)$
2D		X	$S_{imj}^{\rho 2}(C)$

$$(\bar{\rho}^2) = [Z_1\rho^{a0}(R)]^2 + \sum_{l=1}^{3} s^l\Upsilon^l(R) \tag{13}$$

where

$$\Upsilon^l(R) = [\rho^{al+}(R)]^2 - [\rho^{al-}(R)]^2. \tag{14}$$

We call the functions $\Upsilon^l(R)$ the net partial electron densities. The geometric factors Z_1 and s^l for these structures are given in Table II. We will see below that in structures where the second nearest neighbor (2NN) screening parameter $C \leqslant 1$ only 1NN interactions are present. These expressions simplify significantly for the fcc and SC lattices and the difference in the energy *per bond* $(Z_1/2)$ between these structures is given by

$$\Delta E_{SC\text{-}fcc}^{ref}(R) = \frac{1}{6}\{2F[6\rho^{a0}(R)] - F[12\rho^{a0}(R)]\}. \tag{15}$$

Given ρ^{a0} for any initial 1NN distance R_0, we can define a series of 1NN distances R_n through

$$\rho^{a0}(R_n) = \frac{1}{2}\rho^{a0}(R_{n-1}), \tag{16}$$

and iterating Eq. (15) we obtain

$$F[12\rho^{a0}(R_0)] = 2^{N_{max}+1}F[6\rho^{a0}(R_{N_{max}})] - 6\sum_{n=0}^{N_{max}} 2^n \Delta E_{SC\text{-}fcc}^{ref}(R_n). \tag{17}$$

Thus if we knew ρ^{a0}, we could directly obtain the embedding function at any background electron density from the embedding function at a much lower density and the known reference structural energy differences of fcc and SC at specific distances. To obtain an initial estimate for ρ^{a0}, we assume that as, $R \to \infty, \rho^{a0} \to 0$, the scaled embedding function is equal to $A\rho\ln(\rho)$ (see Baskes[5] for the connection of this functional form to the work of Pauling[21]). Using this assumption in Eq. (15), the atomic electron density is given by

TABLE II. Geometric factors for structures considered in this work. Factors given are the number of 1NN Z_1, weighting factors s^l, ratio of 2NN to 1NN distance a, and the screening parameter for 2NN C. Reference structures are denoted by an asterisk.

Structure	Z_l	s^1	s^2	s^3	Z_2	a	C
fcc*	12	0	0	0	6	$\sqrt{2}$	1
hcp*	12	0	0	1/3	6	$\sqrt{2}$	1
o-DC10	10	0	7/24	27/32	4	$\sqrt{3/2}$	5/3
bcc	8	0	0	0	6	$\sqrt{4/3}$	2
t-DC8	8	0	1/6	9/8	12	$\sqrt{2}$	1
SC*	6	0	0	0	12	$\sqrt{2}$	1
t-DC6	6	0	3/32	675/512	4	$\sqrt{3/2}$	5/3
trigonal-6	6	0	8/3	0	6	$\sqrt{4/3}$	2
2D-hex	6	0	6	0	6	$\sqrt{3}$	1/3
DC*	4	0	0	32/9	12	$\sqrt{8/3}$	1/2
2D-square	4	0	8/3	0	4	$\sqrt{2}$	1
beam	4	3	19/6	9/4	2	$\sqrt{3}$	1/3
graphene	3	0	3/2	9/4	6	$\sqrt{3}$	1/3
zigzag-2	2	8/3	8/9	56/27	2	$\sqrt{4/3}$	2
line*	2	0	8/3	0	2	2	0
dimer*	1	1	2/3	2/5	0	—	—

$$\rho^{a0}(R) = \frac{-\Delta E^{ref}_{SC\text{-}fcc}(R)}{2\ln(2)}, \qquad (18)$$

where we have set $A=1$.

We use Eq. (17) to obtain the embedding function, choosing $N_{\max}$ so that $R_{N_{\max}} > 4$. It is trivial to calculate ϕ using Eqs. (12)–(14) and the known reference energy per atom for the fcc structure:

$$\phi(R) = \frac{1}{6}\{E^{ref}_{fcc}(R) - F[12\rho^{a0}(R)]\}. \qquad (19)$$

To obtain Υ^2, note that in Table II, $s^1 = s^3 = 0$ and $s^2 \neq 0$ for the hex, square, and line structures. We choose the line as our reference structure. The energy of this structure is given by

$$E^{ref}_{line}(R) = F[\sqrt{[2\rho^{a0}(R)]^2 + s^2_{line}\Upsilon^2(R)}] + \phi(R). \qquad (20)$$

We solve this equation iteratively for Υ^2 for any R using the previously determined embedding function, ρ^{a0}, ϕ, and the known reference energies. Similarly we get the Υ^3 by using the energy of the hcp structure ($s^3 \neq 0$). Finally, we obtain Υ^1 by using the energy of the dimer structure ($s^1 \neq 0$). These functions are now used to calculate the energy of the DC structure. For scaled $R > 2$ the calculated and known reference data agree well. For $R < 2$ we adjust ρ^{a0} so that the calculated DC energy agrees exactly with the known reference data. Since the embedding function is calculated iteratively [see Eq. (17)], the values at small background electron density (large R) are not affected by changing ρ^{a0} at small R.

The resultant functions are shown in Figs. 1–4. The embedding energy (Fig. 1) is smooth and featureless. The spherically symmetric electron density ρ^{a0}, shown in Fig. 2, is nearly linear (exponential decay) at large scaled 1NN distance, shows a slight positive departure from linearity for $R < 2$, and increases sharply at short 1NN distance. At large distance ρ^{a0} approaches the analytic approximation of Eq. (16). The net partial electron densities are compared in Fig. 3. At short distance [Fig. 3(a)], these net densities ($l = 1-3$) are negative and much smaller in magnitude than the square of the spherically symmetric electron density ρ^{a0}. In Fig. 3(b), it is seen that the magnitude of the angular electron densities decays essentially exponentially at large distance, similar to the behavior of ρ^{a0}. The cusps are due to the change in sign of the net partial electron density. The pair potential [Fig. 4(a)] is smooth and repulsive.

The calculated and known reference energies or energy differences per bond of the reference structures (fcc, SC, line, hcp, dimer, DC) are shown in Figs. 4(a) and 5(a). Note that by construction the known reference and calculated values agree exactly for MS-MEAM. For a simple pair potential model, all energies per bond would equal the pair potential. The deviation of these bond energies from a single curve [Fig. 4(a)] shows the importance of the embedding energy.

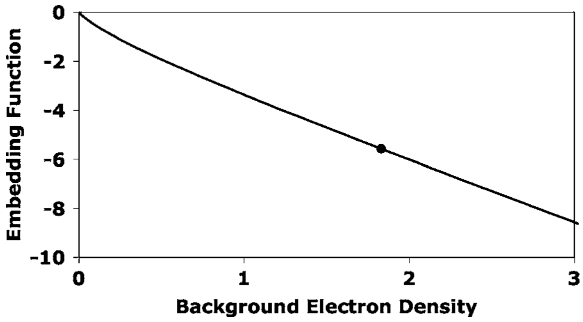

FIG. 1. Embedding energy vs background electron density. The data point denotes the value of the embedding energy at the ground-state equilibrium background electron density.

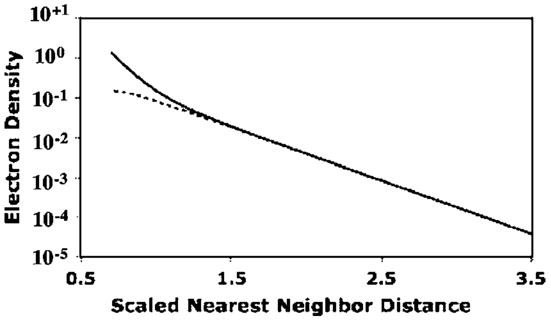

FIG. 2. Spherically symmetric electron density ρ^{a0} (full curve) as a function of scaled 1NN distance. Dashed curve represents the initial approximation [Eq. (18)].

When comparing bonds with equal coordination, it is convenient to look at bond energy differences [Fig. 5(a)], as the bond energies are very close. Any variation from VASP for the hcp-fcc reference structures may be attributed to the initial fit to the VASP database. In summary of this section (see Table I), we have used the six reference structures at 1NN coordination $Z=1-12$ and scaled 1NN distances $R=0.7-4.0$ to determine six of the unknown MEAM functions: embedding energy, pair potential, spherical electron density, and three net partial electron densities.

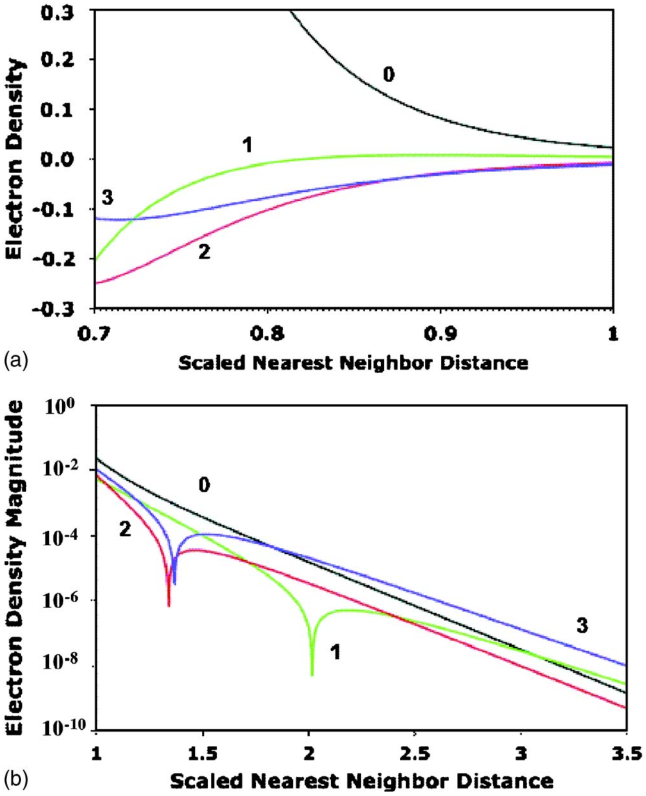

FIG. 3. (Color online) Net partial electron density for $l=1-3$ Υ^l as a function of scaled 1NN distance compared to the square of the spherically symmetric electron density ρ^{a0} (a) at short distance, and (b) the magnitude at long distance.

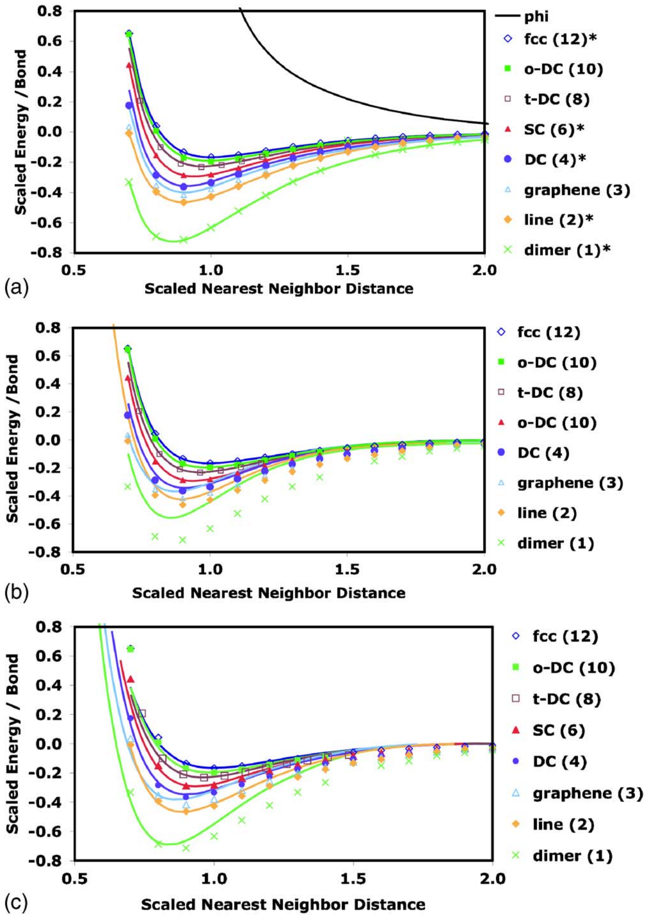

FIG. 4. (Color online) Pair potential and bond energies as a function of scaled 1NN distance for (a) MS-MEAM, (b) EAM (MMPVK) (Ref. 12), and (c) EAM (FBD) (Ref. 11). 1NN coordination is shown in parentheses. Reference structures for MS-MEAM are denoted with an asterisk.

2. The structures with 1NN and 2NN interactions

In order to separate the net partial electron densities into the individual partial electron density contributions, structures that have atom neighbors with at least two distances must be considered. We have attempted to use such structures to determine the partial electron densities, but the structures we have tried are very insensitive to the details of the individual partial electron densities. This insensitivity occurs because the screening of the 2NNs is quite strong. In the future, we intend to try other structure to see if the individual partial electron densities can be determined from the first-principles database. For the purposes of this work, we choose the negative partial electron density as a simple exponential (cf. Appendix A) and calculate the positive partial electron density from

$$\rho^{al+}(R) = \sqrt{\Upsilon^l(R) + [\rho^{al-}(R)]^2}. \tag{21}$$

The exponential is chosen so that the argument of the square root in Eq. (21) is positive for $0.7 < R < 4$. We have not found a property that varies significantly with the choice of this exponential. All of the electron densities are shown in Fig. 6. Their behavior is essentially exponential for $R > 1$.

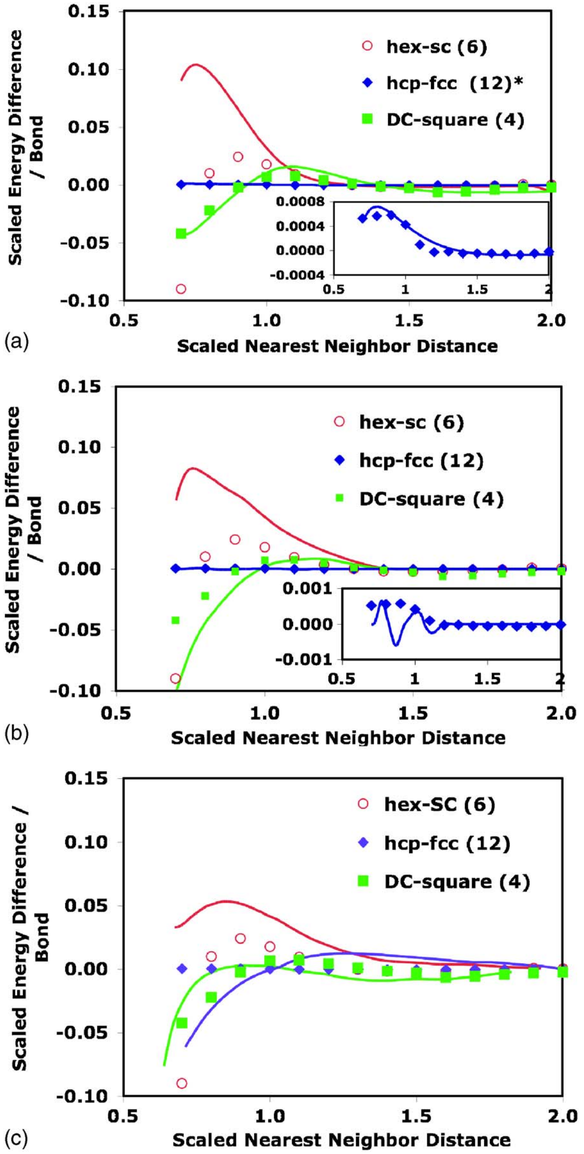

FIG. 5. (Color online) Bond energy differences of structures with equal coordination as a function of scaled 1NN distance for (a) MS-MEAM, (b) EAM (MMPVK) (Ref. 12), and (c) EAM (FBD) (Ref. 11). 1NN coordination is shown in parentheses. Reference structure is denoted with an asterisk. The inset shows the details of the hcp-fcc energy difference.

B. Reference paths

To determine the screening functions we next examine a number of homogeneous transformation paths between the reference structures discussed above as well as two 2D structures, a square lattice (2D-square) and a hexagonal lattice (2D-hex). Details of the transformation paths are given in Appendix B. These transformation paths are analogous to the reference structures used above, and will be called reference paths. The screening functions determine how the bonding changes as the 1NN coordination changes. We use three reference paths to determine the screening functions, the classical Bain path at the equilibrium fcc volume, a 3D trigonal transformation path at the equilibrium fcc volume, and a 2D shear transformation path at a scaled 1NN distance of unity. The Bain path is a constant volume tetragonal distortion from bcc ($c/a=1$) to fcc ($c/a=\sqrt{2}$). The trigonal path may be considered as a constant volume tetragonal distortion of a rotated bcc lattice. Since we will be comparing a number of different transformation paths, we define a fractional deformation, which goes from 0 (bcc) to 1 (fcc) for both the Bain and trigonal paths and from 0.4 (2D-square) to 1 (2D-hex) for the 2D path.

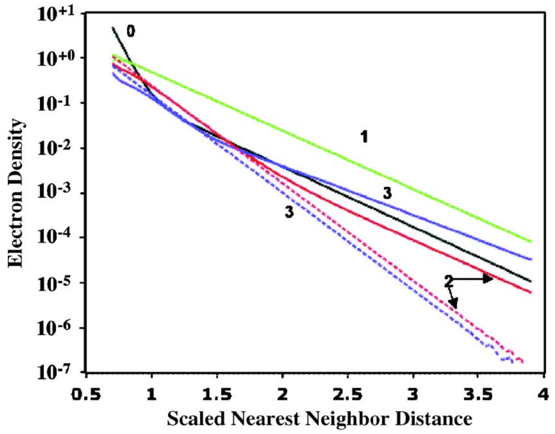

FIG. 6. (Color online) Electron densities for $l=0,3$ as a function of scaled 1NN distance. Full (dashed) lines are the $+(-)$ density.

Along the Bain path at the fcc and bcc structures and along the trigonal path at the fcc, bcc, and SC structures only ϕ and ρ^{a0} enter as functions to be screened. At all other deformations ϕ, ρ^{a0}, and ρ^{a2} enter. We will not consider the screening of ρ^{a1} and ρ^{a3} here; for simplicity, the screening of these atomic electron densities will be taken as that of ρ^{a2}. This assumption is not necessary; use of appropriate reference paths can be used to determine all of the screening functions individually.

In principle, the screening functions S_{imj} for ϕ and ρ are each a function of the vector interatomic distances R_{ij}, R_{im}, and R_{jm}. Previously we have introduced the concept of the screening ellipse[14] and we will use that concept here. Consider that the atom bond ij that is to be screened by atom m lies along the x axis, with the origin of the coordinate system at the bond center. Then an ellipse that goes through all three atoms, i, j, and m, obeys the following equation:

$$x^2+\frac{1}{C}y^2=\left(\frac{1}{2}R_{ij}\right)^2, \tag{22}$$

where the parameter C is given by

$$C=\frac{2(X_i+X_j)-1-(X_i-X_j)^2}{1-(X_i-X_j)^2}, \tag{23}$$

and

$$X_l=\left(\frac{R_{lm}}{R_{ij}}\right)^2, \quad l=i,j. \tag{24}$$

The parameter C indicates the amount of screening: for example, $C=2$ occurs for the 1NN screening of 2NNs in the bcc structure and $C=1$ occurs for the 1NN screening of

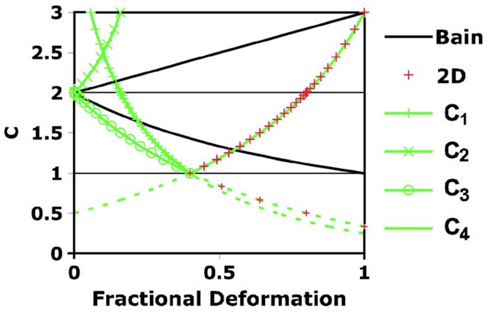

FIG. 7. (Color online) Screening parameter as a function of fractional deformation for the reference paths considered in this work. The Bain, 2D, and trigonal paths are used to determine the screening functions. See Appendix B for a discussion of the trigonal screening parameters (green).

2NNs in the SC, 2D-square, and fcc structures (see Table II). For any amount of fractional deformation, we can calculate the C values that enter into the screening. Details are given in Appendix B. These C values are shown in Fig. 7. This figure is simply a result of the geometry along the reference paths. The 2D path represents the simplest screening. At the square lattice ($f=0.4$), the four 2NNs all have $C=1$. As the lattice is sheared (increasing f) C increases smoothly to 3, as two of the 2NNs become 1NNs and decreases to 1/3 for the other two 2NNs. Hence, along this path, the coordination changes from 4 (2D-square) to 6 (2D-hex). A similar process occurs for the Bain path, where four bcc 2NNs become 1NNs in fcc. The screening along the trigonal path is much more complicated, where six different screening environments occur. As discussed in Appendix B, we can simplify the trigonal screening significantly by assuming that for $C<1$ the screening is complete, i.e., $S_{imj}=0$. This assumption is consistent with having only 1NN interactions in fcc, SC, and the 2D-square lattice. When this assumption is made, only the full lines for the trigonal screening enter; the dashed lines do not play a role.

The philosophy for determining the screening functions is exactly the same as that used above to determine the other MEAM functions, i.e., for each C we determine the three unknown S_{imj} (for ϕ, ρ^{a0}, and ρ^{a2}) using three points along the transformation paths simultaneously. We first determine the screening for $C=2$. This value of C occurs for the bcc structure ($f=0$) and for another point along both the trigonal path ($f=0.8$) and the 2D deformation path ($f=0.8$). Using the known reference energies for these three structures, we obtain $S_{imj}^{\phi}(2)$, $S_{imj}^{\rho_0}(2)$, and $S_{imj}^{\rho_2}(2)$. We now determine the screening at $C=1.5$. From Fig. 7 we see that for the trigonal and 2D paths at $f=0.64$ and for the trigonal path at $f=0.16$ the screening parameter is 1.5. As above, we obtain S_{imj}^{ϕ} (1.5), $S_{imj}^{\rho_0}$ (1.5), and $S_{imj}^{\rho_2}$ (1.5). The MS-MEAM and VASP energies at the endpoints of the 2D transformation (2D-square and 2D-hexagonal) do not agree exactly, since these structures are not reference structures. To facilitate the determination of the screening functions between the endpoints, the energies relative to the endpoints are used for both MS-MEAM and VASP.

Now, assuming smooth screening functions for $C>2$ that go through the values just determined at $C=2$, we determine the screening for $C<2$ using the 2D and trigonal data for $f<0.72$ and the trigonal data for $f>0$. Finally, we determine the screening for $C>2$ using the 2D and trigonal data for $f<0.72$ and the Bain transformation data for all f. The process is then iterated until convergence.

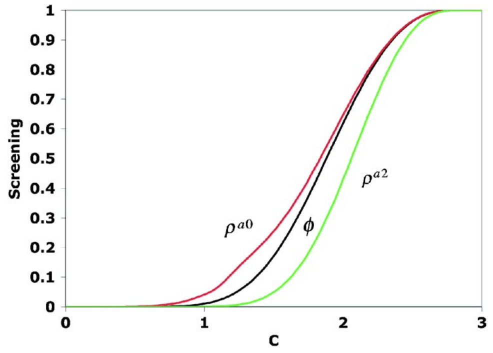

FIG. 8. (Color online) Screening function for the pair potential ϕ and atomic electron densities ρ^{al} vs the screening parameter C.

The resultant screening functions are shown in Fig. 8. Note that the screening functions for ϕ and ρ^{a0} are similar at high C, while the screening function for ρ^{a2} falls off more rapidly with decreasing C. Our previous work assumed that the screening for all functions was identical. This work shows that the previous assumption was close, but not exact. It is shown in Fig. 9 that the resultant energetics for MS-MEAM agrees almost perfectly with the VASP database for the reference paths.

IV. MODEL PREDICTIONS

There are two ways to investigate the robustness of our MS-MEAM functions. The first is to compare predictions of

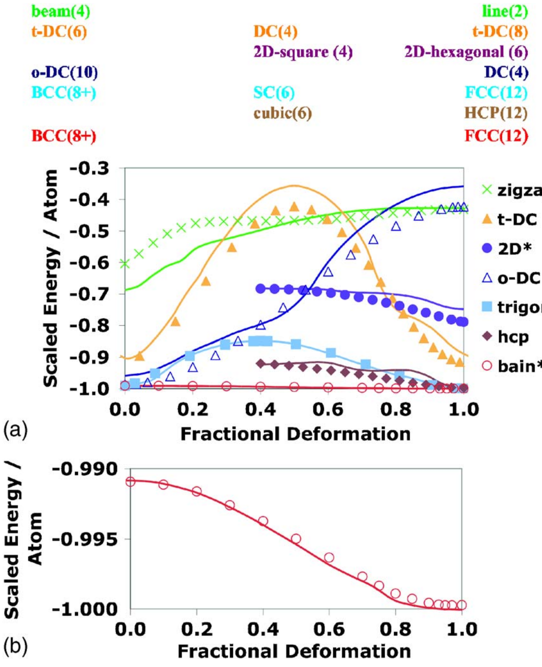

FIG. 9. (Color online) Predicted (line) and first-principles (points) scaled energies as a function of fractional deformation along (a) various paths, and (b) Bain path (expanded view). Reference paths are denoted with an asterisk.

TABLE III. Comparison of energy E and first neighbor distance r_1 for equilibrium structures. The fcc energies (eV/atom) are relative to isolated atoms at infinity and the fcc 1NN distance is in Å. The energies and 1NN distances of other structures are normalized by the fcc energy and the fcc 1NN distance. Structures designated with an asterisk are MS-MEAM reference structures. MS-MEAM values have been unscaled by 3.54 eV and 2.56 Å, the experimental values of the fcc cohesive energy and 1NN distance. For MS-MEAM, the c/a relative to ideal is 1.008, the volume is 0.9997 relative to ideal hcp and the energy is 0.3 meV lower. Differences in energies between VASP and MS-MEAM may be attributed to the scaling procedure.

Structure	VASP		MS-MEAM		EAM (MMPVK)		EAM (FBD)	
	E	r_1	E	r_1	E	r_1	E	r_1
fcc*	−3.731	2.571	−3.540	2.560	−3.540	2.560	−3.540	2.560
hcp	0.998	0.999	0.997	0.998	0.998	0.998	0.999	0.998
hcp* (c/a ideal)	0.998	1.000	0.997	1.000	0.998	1.000	0.999	1.000
bcc	0.991	0.978	0.989	0.976	0.987	0.970	0.992	0.971
o-DC10	0.980	0.992	0.959	0.986	0.685	0.906	0.696	0.904
trigonal-6			0.956	0.930	0.956	0.964	0.958	0.948
t-DC6			0.907	0.929	0.912	0.939	0.915	0.936
t-DC8			0.905	0.966	0.925	0.960	0.925	0.957
SC*	0.878	0.938	0.878	0.938	0.878	0.935	0.877	0.932
2D-hex	0.809	0.951	0.749	0.991	0.717	0.961	0.737	0.961
DC*	0.727	0.903	0.717	0.910	0.685	0.906	0.696	0.904
2D-square	0.730	0.916	0.713	0.931	0.662	0.927	0.703	0.911
beam			0.693	0.982	0.597	0.940	0.625	0.930
zigzag-2			0.681	0.923	0.568	0.895	0.599	0.884
graphene	0.627	0.912	0.600	0.904	0.550	0.907	0.576	0.898
line*	0.464	0.897	0.464	0.897	0.423	0.893	0.467	0.884
dimer*	0.362	0.860	0.362	0.860	0.278	0.855	0.346	0.838

the model with additional VASP calculations not used in the function development, and the second is to compare the model calculations with experiment. We use the latter comparisons where the VASP calculations are too computationally expensive to perform. Of course, the latter comparison has the disadvantage that the VASP model itself may not predict experiment correctly.

At this juncture it is appropriate to comment on the speed of the MS-MEAM code. A highly optimized parallel MEAM code runs 3–5 times slower than an EAM code. A MS-MEAM code should in principle run as fast as the traditional MEAM code. However, our poorly optimized research code for MS-MEAM runs about 10 times slower than our MEAM code.

A. Comparison with first-principles calculations

We first use the functions developed above to predict the energetics of a number of structures with a wide range of 1NN coordination. The results are shown in Figs. 4(a) and 5(a) and Table III. The graphene (one plane of graphite) structure has a 1NN coordination of three. The predicted energy as a function of 1NN distance agrees extremely well with the VASP calculation. We discuss an orthorhombic transformation of the DC structure below and in Appendix B. One point along this deformation path is a tenfold coordinated structure we call *o*-DC10. The predicted energy of this structure as a function of 1NN distance also agrees well with the VASP calculations. Similarly, we have examined a tetrahedral distortion of the DC structure (see below and Appendix B for details of the transformation). Along this path, there is an eightfold coordinated structure we call *t*-DC8 (see Fig. 16 in Appendix B). Again, the MS-MEAM predictions agree well with the first-principles calculations. We also have calculated the energy difference between structures with the same 1NN coordination. These energy differences are very small and the demands on the model are severe. The comparison of the DC and 2D-square configurations (Z=4) shows good agreement with VASP at all 1NN distances, while the 2D-hex/SC (Z=6) and the *t*-DC6/SC (Z=6) comparison shows some disagreement at small 1NN distance. Thus, we may conclude that the MS-MEAM agrees well with the first-principles energy/volume calculations for 1NN coordination ranging from 1–12 at most 1NN distances.

For comparison, we also present results for two literature EAM potentials for Cu: the original potential by Foiles *et al.*[11] (FBD) and a more recent potential by Mishin *et al.*[12] (MMPVK). FBD used a small data set of experimental information to develop the potential, while Mishin *et al.* used a large database of first-principles calculations and experiment to fit their potential. The results are also presented in Figs. 4 and 5. The MMPVK EAM potential represents the VASP data quite well at high coordination, but has significant deviation at lower coordination. The FBD EAM potential does surprisingly well near equilibrium for all coordinations even though no low coordination data was used in its development. It misses the behavior of the low coordination structures at low density and is too soft at high density. Both

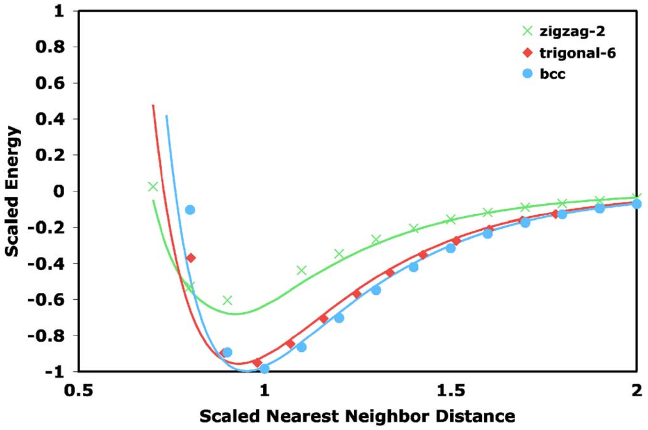

FIG. 10. (Color online) Predicted (line) and first-principles (points) scaled energies as a function of scaled 1NN distance. One point of the bcc curve was used as a reference structure.

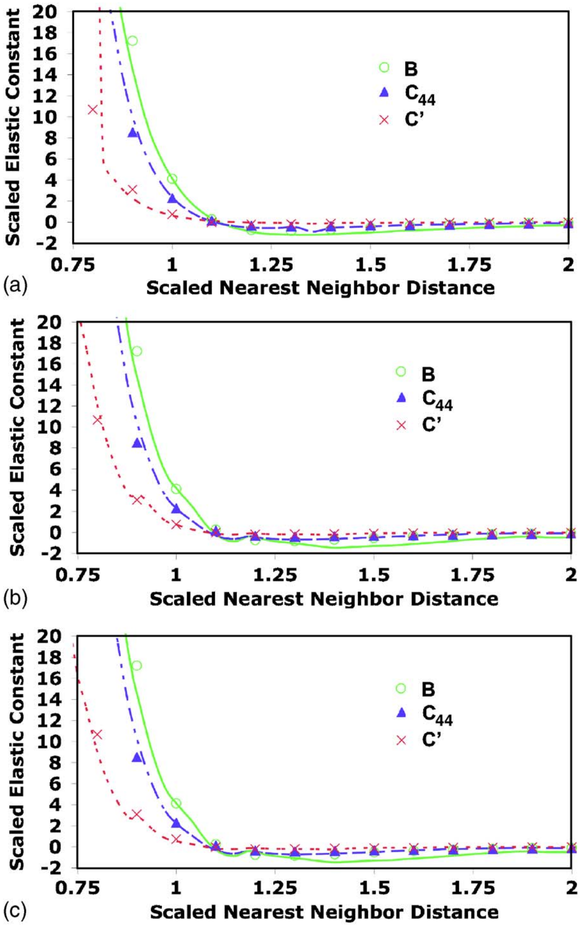

FIG. 11. (Color online) Scaled elastic constants for fcc vs scaled 1NN distance for a) MS-MEAM, (b) EAM (MMPVK) (Ref. 12 and (c) EAM (FBD) (Ref. 11) Points are the VASP calculations.

EAM potentials capture the qualitative behavior of the energy difference between structures with the same 1NN coordination, but clearly are far from quantitative. The MMPVK potential shows significant oscillations in the energy difference between hcp and fcc at high densities. The FBD EAM potential does not give even qualitative agreement with the VASP database for the hcp/fcc energy difference. It is well known that this potential does not reproduce the related stacking fault energy very well.

The comparisons above are all for structures with only 1NN interactions. In Fig. 10 we present the comparison of energy vs scaled 1NN distance for three structures where 2NN interactions are of some importance, bcc, a point along the trigonal deformation path called trigonal-6, and a point along a path called zigzag-2 (discussed below). In Table II we see that these structures have the largest value of the screening parameter C and hence, the largest contribution of 2NN interactions. The trigonal-6 structure may be thought of as compressing an fcc structure along the [111] axis so that the out-of-plane neighbors are closer than the in-plane neighbors by the factor given in Table II. Similarly, the zigzag-2 structure has the same 1NN/2NN distance ratio. The MS-MEAM prediction is in excellent agreement with the VASP database except at very short distances (>50% volume compression). This agreement justifies the assumption made above in Sec. III B that the angular screening is independent of distance.

Elastic constants are important quantities for atomistic calculations. Both EAM potentials used equilibrium elastic constants as direct input to the model, while the MS-MEAM included elastic constant information through the transformations. The predicted elastic constants for fcc for all three models as a function of 1NN distance are compared with VASP in Fig. 11. All three models represent the VASP database quite well.

Deformations are an extremely sensitive measure of the predictive capability of the model. Using a shear transformation analogous to the 2D transformation, we have calculated the energetics of a homogeneous transformation of hcp to a cubic structure through shear parallel to the basal plane. This calculation starts with an hcp structure with ideal c/a ratio, scaled 1NN distance equal to unity, and maintains constant volume by adjusting the c/a ratio as the lattice is sheared. This path is called hcp in Fig. 9. MS-MEAM is in excellent agreement with VASP, although it has some small oscillations, most likely due to the screening function. We have also looked at a tetragonal transformation (t-DC) of the DC lattice (in cube orientation). Starting with a DC structure with the scaled 1NN distance equal to unity, straining to larger c/a ratios yields a structure t-DC8 at $(\frac{c}{a})^3=6$ with eight 1NN, while straining to smaller c/a ratios yields a structure t-DC6 at $(\frac{c}{a})^3=\frac{2}{15}$ with six 1NN (see Fig. 16 in Appendix B). These symmetric structures are shown in Appendix B. While the MS-MEAM is not in quantitative agreement with VASP, the basic trend of the energy curve is in agreement with the first-principles calculation.

It is also possible to transform the DC structure to a structure that has ten 1NN as mentioned above (o-DC). The details of this transformation are given in Appendix B. The volume is held fixed at the equilibrium fcc volume for this transformation. The MEAM prediction is in reasonable agreement with the first-principles calculation for this path.

Finally, we consider a homogeneous transformation with low coordination that we call the zigzag transformation. Consider a line of atoms (Fig. 12) with the scaled 1NN dis-

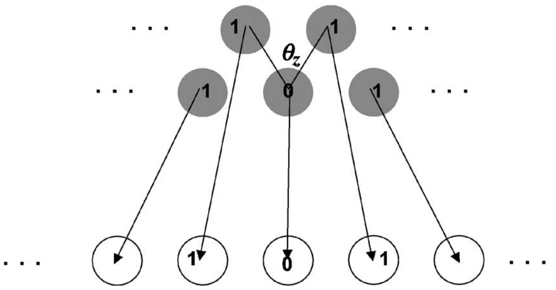

FIG. 12. Schematic of the zigzag transformation. The beam structure (gray) is transformed to a line (open). Atoms labeled 1 are 1NN to the atom labeled 0. Arrows denote the atom path as a function of the transformation parameter θ_z. The zigzag-2 structure occurs for $\cos(\theta_z)=\frac{1}{3}$.

tance between atoms equal to unity. Now place a second such line parallel to the first line, so that each atom is at the vertex of an equilateral triangle. We call this the beam configuration, and each atom has four 1NNs and the angle between 1NN atoms is $\theta_z=60°$. The periodic distance along the line is $2\sin(\theta_z)$ and the distance between the lines is $\cos\left(\frac{\theta_z}{2}\right)$. As θ_z is increased from 60° to 180°, the beam is stretched into a single line with 1NN coordination equal to two. For the beam, the agreement with VASP is excellent. Since the line was fit, we expect (and obtain) perfect agreement. Along this transformation path the scaled 1NN distance is held fixed at unity. The agreement with the VASP calculations is only fair for this path. A significant disagreement is found near the fractional deformation of 0.25 ($\theta_z=90°$, $C=1$). To obtain agreement with VASP, we would have to have stronger interactions at this C. Such a change is beyond the scope of this work, but is necessary if MS-MEAM is to be applied to transformations of very low coordination structures. Apparently, the inclusion of the dimer reference structure is not sufficient; bond breaking between singly and doubly coordinated structures must be included.

We now examine the behavior of the two literature EAM potentials for the same transformations. The results are presented in Figs. 13 and 14. The agreement of both EAM potentials with VASP is excellent for the higher coordination transformations. However, for the lower coordinations, 2D and zigzag, the agreement is not very good. Both potentials predict the maximum in the *t*-DC transformation to be at lower deformation than the VASP database. For the Bain paths, the bcc energy is in disagreement with VASP, but the shape of the transformation curve is in reasonable agreement with VASP.

An important deformation path for mechanical properties of fcc materials is slip in a ⟨112⟩ direction in a (111) plane. This deformation path is called the generalized stacking fault (GSF). The unrelaxed GSF energy has previously been calculated[22] using DFT and the data is reproduced here in Fig. 15 along with the MS-MEAM results and the results from the two literature EAM potentials. At a fractional deformation of zero, the structure is fcc and at a fractional deformation of unity, a stacking fault is formed. The maximum half way through the path is called the unstable stacking fault (USF). The stacking fault energy (SFE) predicted by MS-MEAM is in excellent agreement with the DFT calculation because the SFE is closely related to the hcp/fcc energy difference, which is part of the VASP database. The predicted USF energy is not in very good agreement with the DFT calculation. The MMPVK EAM potential is fit to the SFE; thus, it has excellent agreement. Surprisingly, the GSF for the FBD EAM potential is almost identical to that of the MMPVK EAM potential.

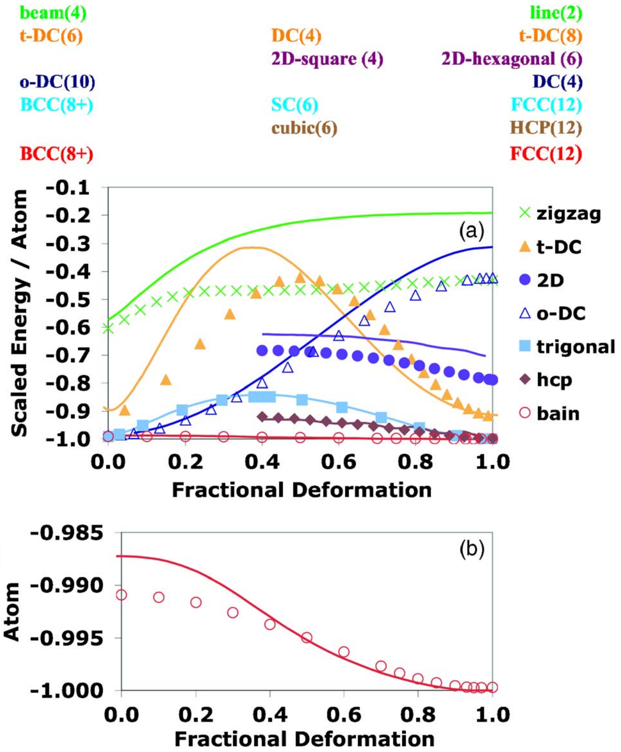

FIG. 13. (Color online) MMPVK (Ref. 12) EAM (line) and first-principles (points) scaled energies as a function of fractional deformation along (a) various paths, and (b) Bain path (expanded view).

B. Comparison with experiment

As to the more complicated tests of the model, we have calculated a number of defect and thermodynamic properties. The results are given in Tables IV and V. To compare with experiment, the MS-MEAM results are unscaled by the experimental cohesive energy (3.54 eV) and the experimental 1NN distance (2.56 Å). In general, there is not much difference between the three potentials and agreement with experiment is reasonably good, but certainly not quantitative. If any conclusion can be made, the MS-MEAM potential has slightly poorer agreement with experiment, most likely because no experimental data was used in its derivation. There are no critical problems with any of the three potentials. We are somewhat disappointed by the lack of quantitative agreement between MS-MEAM and experiment. Whether this disagreement is due to a deficiency in the MS-MEAM formalism or in the VASP database remains a subject for future study.

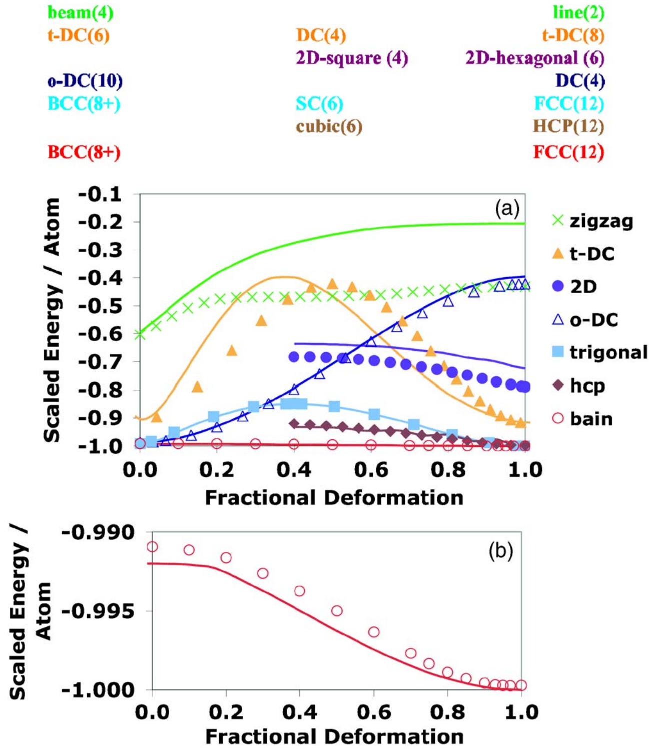

FIG. 14. (Color online) FBD (Ref. 11) EAM (line) and first-principles (points) scaled energies as a function of fractional deformation along (a) various paths, and (b) Bain path (expanded view).

V. SUMMARY

Formalism has been developed to determine MEAM functions directly from a first-principles database. The method presented here uses first-principles energy vs volume calculations for a series of crystal structures that span nearest neighbor coordinations of 1–12. In addition, first-principles data along transformation paths connecting these structures are used. The resultant MEAM functions for a model material Cu reproduce the database of VASP calculations exactly (by construction) and also predict additional first-principles calculations. The model is also used to predict a large number of complex properties, which are in reasonable agreement with experiment. We believe that this formalism produces a computationally efficient potential that is largely a quantitative interpolation of any first-principles database. Application of this formalism to multicomponent materials systems could enable the long-promised goal of quantitatively predictive computational materials science. Towards this end, we are developing a MS-MEAM model for hcp-Zr.

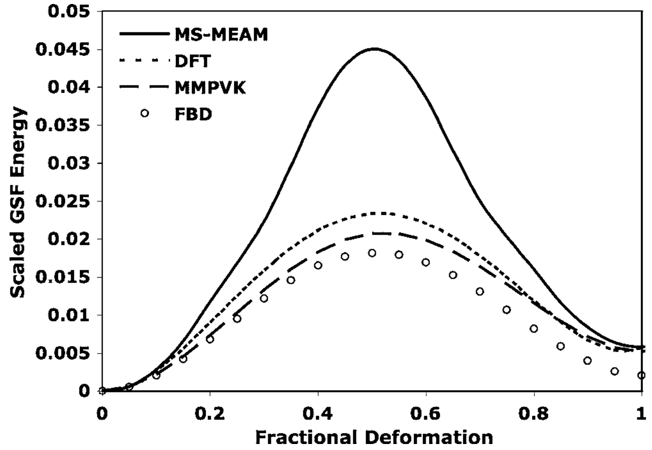

FIG. 15. Scaled fault energy for unrelaxed shear of a (111) surface in ⟨211⟩ angle direction as a function of fractional deformation. Multiply the energy values by 8643 to convert them to mJ/m^2.

ACKNOWLEDGMENTS

The authors would like to acknowledge the financial support of the U. S. DOE through the Office of Science, Office of Basic Energy Sciences and the ASC and ESC programs at Los Alamos National Laboratory (LANL). Fruitful discussions with Joel Kress and Michael Demkowicz at LANL are also very much appreciated.

APPENDIX A

A typical expression for an electron density consisting of two contributions is

$$\rho(\vec{r}) = \frac{\rho^u(\vec{r};V) + \lambda^2\rho_2(\vec{r})}{1+\lambda^2} = \rho^u(\vec{r};V) + \frac{\lambda^2}{1+\lambda^2}[\rho_2(\vec{r}) - \rho^u(\vec{r};V)], \tag{A1}$$

where $\rho(\vec{r})$ is the electron density at any point in space $\vec{r}$ for the current configuration $\{\vec{R}_i\}_{i=1,\ldots,N}$ and $\rho^u(\vec{r};V)$ is the electron density for a reference configuration of volume V. $\rho_2(\vec{r})$ is a second density contribution that contains deviations from the reference structure. Because λ is assumed to be optimized for each configuration, it will depend on the $\{\vec{R}_i\}$. Thus the $\lambda^2\rho^u(\vec{r};V)/(1+\lambda^2)$ density contribution is not precisely the same as the contribution $\rho^u(\vec{r};V)$ itself. It is then natural to view the background density Eq. (4) as having the same form as Eq. (A1) with three independent contributions. Keep in mind that $\rho^u(\vec{r};V)$ exists for each point on the reference curve V, e.g., V may represent a specific atomic volume. Knowing the average atomic volume in the current configuration, we choose that volume on the reference curve.

Further, suppose that each constituent density can be represented by a single determinant wave function composed of one-electron spatial orbitals. In this case, an electron density can be represented as a sum of squares of the spatial orbitals χ_m, all with equal weight:

$$\rho(\vec{r}) = \sum_{m=1}^{M} \chi_m(\vec{r})^2. \tag{A2}$$

The sum is over all M electrons in the system. An analogous expression holds for ρ^u. The difference between the two electron densities then becomes

$$\rho_2(\vec{r}) - \rho^u(\vec{r}) = \sum_{m=1}^{M} [\chi_{2m}(\vec{r})^2 - \chi_m^u(\vec{r})^2]. \tag{A3}$$

TABLE IV. Calculated defect properties of fcc Cu at T=0 K compared to experiment. Values denoted by an asterisk were fitted. MS-MEAM values have been unscaled by 3.54 eV and 2.56 Å, the experimental values of the fcc cohesive energy and 1NN distance.

Property	MS-MEAM	FBD[a]	MMPVK[b]	Experiment
Stacking Fault energy (mJ-m^{-2})	49.6	17.35	36.2	45.0[b]
Coherent-twin boundary energy (J-m^{-2})	24.9	8.73	22.2	24.0[b]
(100) surface energy (J-m^{-2})	1.11	1.29	1.34	
(110) surface energy (J-m^{-2})	1.05	1.18	1.23	1.79[c]
(111) surface energy (J-m^{-2})	1.37	1.42	1.47	
(100) surface layer relaxation (%)	−1.7	−1.4	−1.7	−1[d]
(111) surface layer relaxation (%)	−3.4	−1.3	−1.7	−1[d]
(110) surface layer relaxation (%)	+0.1	−0.1	−0.2	−5−−8[e]
Unrelaxed vacancy formation energy (eV)	1.06	1.32	1.30	
Relaxed vacancy formation energy (eV)	1.02	1.28*	1.26*	1.15–1.30[e]
Vacancy formation volume (Ω)	0.89	0.74	0.71	0.78[f]
Relaxed vacancy migration energy (eV)	0.99	0.66	0.69	0.71[b]
[100] split self-interstitial formation energy (eV)	2.58	2.86	3.06	
[100] split self-interstitial formation volume (Ω)	0.24	0.72	0.82	0.55±0.20[g]
Relaxed octahedral self-interstitial formation energy (eV)[h]	3.44	unstable	unstable	
Relaxed [110] split self-interstitial formation energy (eV)	2.45	3.05	3.30	

[a] Reference 11.
[b] Reference 12.
[c] Reference 23 (polycrystalline average).
[d] See references in Ref. 11.
[e] References 24 and 25.
[f] Reference 26.
[g] Reference 27.
[h] The O_h interstitial relaxes to an off-center position for MS-MEAM and to the [100] split interstitials for the EAM potentials.

If the current system configuration does not deviate too drastically from that reference state, the core orbitals of the current configuration will not differ from the reference state. These core orbitals may be removed from the density difference. In the simplest approximation, we retain only one orbital, say the M^{th} orbital, so that $\rho_2-\rho^u\approx\chi_M^2-\chi_M^{u2}$.

Next, we assume that it is possible to expand both χ_M and χ_M^u in some common, primitive atomic basis set ρ^a: $\chi_N(\vec{R})\approx\Sigma_j C_j\rho^a(\vec{R}-\vec{R}_j)$ and $\chi_N^u(\vec{r})\approx\Sigma_j C_j^u\rho^a(\vec{r}-\vec{R}_j)$. Then ρ_2 takes the approximate form

$$\rho_2 \approx \sum_{jk} C_j C_k \rho_2^a(\vec{r}-\vec{R}_j)\rho_2^a(\vec{r}-\vec{R}_k). \tag{A4}$$

A completely analogous approximation also holds for $\rho^u(\vec{r};V)$. We are interested in this density difference at a specific atom i; thus we set $\vec{r}=\vec{R}_i$. If we can separate the radial and angular dependence of ρ^a as a product, we take

$$\rho^a(\vec{R}_{ij}) \approx \sum_l \rho^{al}(R_{ij})\Xi^{al}(\Omega_{ij}), \tag{A5}$$

where $\Xi(\Omega)$ represents the angular dependence referenced to the axis defined by $\vec{R}_i-\vec{R}_j$. Then using a Legendre expansion, the terms in Eq. (A4), scaled by $\lambda^2/(1+\lambda^2)$, become

$$\sum_l B_{ijk}^l \rho^{al}(R_{ij})\rho^{al}(R_{ik})P_0^l[\cos(\theta_{jki})], \tag{A6}$$

where

$$B_{ijk}^l = \left\langle \frac{\lambda^2 C_j C_k \Xi^{al}(\Omega_{ij})\Xi^{al}(\Omega_{ik})}{1+\lambda^2} \middle| P_0^l[\cos(\theta_{jki})] \right\rangle. \tag{A7}$$

The angular brackets indicate local angular averages about the angle of interest. Substituting Eq. (A6) into Eq. (A4) and switching the order of the summations, we obtain

$$\frac{\lambda^2\rho_2}{1+\lambda^2} \approx \sum_l \sum_{jk} B_{ijk}^l \rho^{al}(R_{ij})\rho^{al}(R_{ik})P_0^l[\cos(\theta_{jki})]. \tag{A8}$$

Comparing Eq. (A8) with Eq. (5b), we see that the product of the screening functions is analogous to the quantity B,

$$B_{ijk}^l \leftrightarrow S_{ij}^{\rho l} S_{ik}^{\rho l}. \tag{A9}$$

The screening functions appear as estimates of the optimal expansion coefficients, but also include factors related to the Legendre coefficients of both the expansion coefficients

TABLE V. Comparison of calculated thermodynamic properties of fcc and liquid Cu at various temperatures T. MS-MEAM values have been unscaled by 3.54 eV and 2.56 Å, the experimental values of the fcc cohesive energy and 1NN distance.

Property	T(K)	MS-MEAM	FBD[a]	MMPVK[b]	Experiment[c]
			fcc		
Linear thermal expansion coefficient (ppm-K^{-1})	300	15.5	16.8	16.4*	17.0
	1273	28.2	29.1	29.5	20.3
Specific heat (J-kg^{-1}-K^{-1})	300	414	405	403	386
	1310	498	517	524	473
			fcc/liquid		
Melting point (K)		1570	1282	1331	1357
Latent heat of melting (kJ-mol-1)	1350	16.6	11.13	11.75	13.02
Relative volume change on melting (%)	1350	9.1	4.59	4.97	4.20
Pressure derivative of melting (K-GPa^{-1})	1350	104	28	31	35[d]
			liquid		
Specific heat (J-kg^{-1}-K^{-1})	1500	601	558	543	495
Density (c-cm^{-3})	1350	7.68	7.88	7.87	8.0
Temperature derivative of density (mg-cm^{-3}-K^{-1})	1425	−1.23	−0.89	−0.79	−0.80
Surface tension (mN-m-1)	1356	210	1092	1182	1285
Temperature derivative of surface tension (mN-m^{-1}-T^{-1})	1356	0.00	−0.27	−0.20	−0.13

[a] Reference 11.

[b] Reference 12.

[c] Reference 28.

[d] Reference 29.

and the primitive basis functions. The factored form of the expansion coefficients is used to keep the component-dependence pair wise. (Otherwise, it would be necessary to have density screening factors with three indices $S_{ikj}^{\rho_l}$, which would be computationally much more demanding.) It is through this set of approximations that EAM and MEAM models attempt to avoid the variational determination of $\bar{\rho}$. Hence, there is no requirement that the functional forms for the energy be variational in $\bar{\rho}$. Historically, these density expressions have always been associated with $\bar{\rho}^2$ instead of just $\bar{\rho}$.

APPENDIX B

We present here the details of the transformation paths and the relationships between the screening and the reference paths.

1. Bain path

The Bain path is most simply characterized by the c/a ratio ranging from 1 at bcc to $\sqrt{2}$ for fcc. The transformation is characterized by

$$a = a_0\left(\frac{c}{a}\right)^{(-1/3)}, \tag{B1}$$

$$c = a_0\left(\frac{c}{a}\right)^{(2/3)}, \tag{B2}$$

where $a_0=2^{1/6}$. We define the fractional deformation along the Bain path by

$$f = \left(\frac{c}{a}\right)^2 - 1. \tag{B3}$$

For each point along the Bain path, there are two relevant screening parameters:

$$C_1^{Bain} = 2 + f, \tag{B4}$$

$$C_2^{Bain} = \frac{2}{1+f}. \tag{B5}$$

2. 2D path

The 2D path is characterized by an angle θ between 1NNs which varies from 60° for the hexagonal structure [a single (111) plane in fcc] to 90° for the square structure [a single (100) plane in SC]. The basis vectors along this path are given by (1,0) and $[\sin(\theta), \cos(\theta)]$. The fractional deformation is defined as

$$f = \frac{2}{5}[1 + 3\cos(\theta)]. \tag{B6}$$

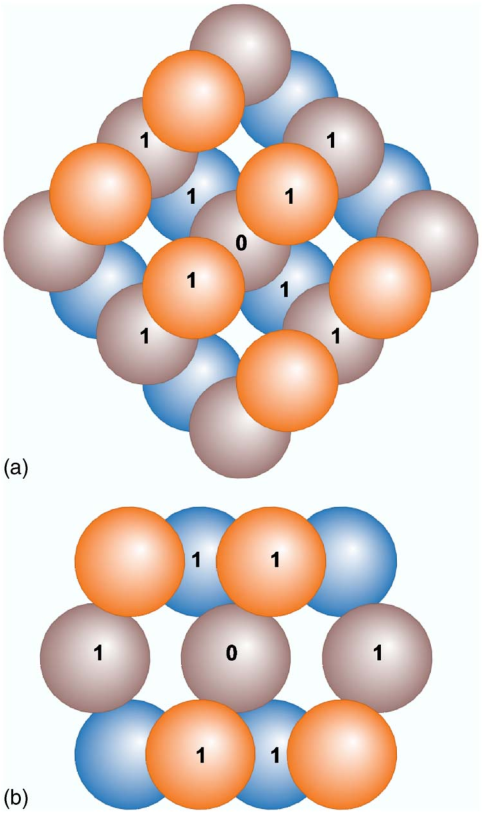

FIG. 16. (Color online) Structure (a) *t*-DC8 formed by the tetragonal distortion of the DC lattice with $(c/a)^2=6$, and (b) *t*-DC6, $(c/a)^2=2/15$. For *t*-DC8, the atom labeled 0 has eight 1NN (labeled 1) and twelve 2NN (unlabeled). For *t*-DC6, the atom labeled 0 has six 1NN (labeled 1) and four 2NN (unlabeled). Colors denote depth in the figure.

For each point along the 2D path there are two screening parameters given by

$$C_1^{2D} = \frac{1+\cos\theta}{1-\cos\theta} = \frac{4+5f}{8-5f}, \tag{B7}$$

$$C_2^{2D} = \frac{1}{C_1^{2D}}. \tag{B8}$$

3. Trigonal path

The trigonal path has been described previously by Paidar *et al.*[30] and may be considered as a constant volume tetragonal distortion of a bcc lattice whose x, y, and z axes are parallel to the $[1\bar{1}0]$, $[11\bar{2}]$, and $[111]$ directions, respectively. The transformation is characterized by

$$a = a_0\sqrt{2}p^{(-1/3)} \tag{B9}$$

$$b = a_0\sqrt{6}p^{(-1/3)} \tag{B10}$$

$$c = a_0\frac{\sqrt{3}}{2}p^{(2/3)}, \tag{B11}$$

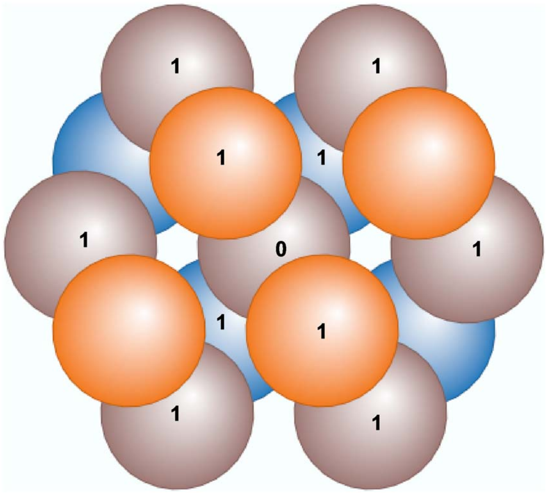

FIG. 17. (Color online) Structure *o*-DC10 formed by the octahedral distortion of the DC lattice by an angle of 60° in Eq. (B9). The atom labeled 0 has ten 1NN (labeled 1) and four 2NN (unlabeled). Colors denote depth in the figure.

where a_0 is the lattice constant of the bcc lattice defined above and p is a parameter. When $p=1$, 2, *or* 4 the structure is bcc, SC, or fcc, respectively. A more physical description of the transformations is through the angle θ between 1NN:

$$\cos(\theta) = \frac{p^2-4}{p^2+8}. \tag{B12}$$

The fractional deformation is given by Eq. (B4) above. Unfortunately, the trigonal path has six screening parameters associated with it. Fortunately, the net screening factor for any two atoms consists of a product of screening factors [see e.g., Eq. (3)] and frequently the screening parameters are small, leading to complete screening. If we assume that for $C<1$ the screening is complete, i.e., $S_{imk}=0$, then only four screening factors are relevant and they are given by

$$C_1^{trig} = \frac{1-\cos\theta}{1+2\cos\theta} = \frac{8-5f}{2+10f} \tag{B13}$$

$$C_2^{trig} = \frac{\cos\theta-1}{2\cos\theta} = \frac{8-5f}{4-10f} \tag{B14}$$

$$C_3^{trig} = C_2^{2D} \tag{B15}$$

$$C_4^{trig} = C_1^{2D}. \tag{B16}$$

4. DC-tetragonal path

Another path that we consider is a tetragonal deformation of the DC structure. Two symmetric structures occur along this path: for $(c/a)^2=6$ a structure with eight 1NN, *t*-DC8 and for $(c/a)^2=2/15$ a structure with six 1NN, *t*-DC6 (Fig. 16). For *t*-DC8 each 2NN is screened by two 1NN with $C=1$ and for *t*-DC6 each 2NN is screened by two 1NN with $C=5/3$. The fractional deformation is taken as a linear function of $(c/a)^{1/3}$ ranging from 0 at *t*-DC8 to 0.45 at DC to 1 at *t*-DC6. The transformation is at constant volume.

5. DC-orthorhombic path

It is also possible to perform an orthorhombic transformation of the DC structure to a structure that has ten 1NN *o*-DC10 (Fig. 17). The transformation may be characterized by an angle θ, 60° (*o*-DC10) $<\theta<$ 90° (DC). The orthorhombic deformations are given by

$$\delta_x = \omega(\theta)\sin(\theta)[1-\cos(\theta)]$$

$$\delta_y = \omega(\theta)[1-\cos(\theta)/2]$$

$$\delta_z = \omega(\theta)\sqrt{3-\delta_x^2-\delta_y^2}. \tag{B17}$$

For $\omega=1$ the scaled 1NN distance is fixed and for ω chosen so that $\delta_x\delta_y\delta_z=1$, the transformation is at constant volume. We consider only the constant volume transformation here. The fractional deformation is taken as a linear function of θ ranging from 0 at *o*-DC10 to 1 at DC.

---

*Electronic address: baskes@lanl.gov

[1] M. S. Daw and M. I. Baskes, Phys. Rev. B **29**, 6443 (1984).

[2] M. S. Daw and M. I. Baskes, Phys. Rev. Lett. **50**, 1285 (1983).

[3] F. Ercolessi, E. Tosatti, and M. Parrinello, Phys. Rev. Lett. **57**, 719 (1986).

[4] M. W. Finnis and J. E. Sinclair, Philos. Mag. A **50**, 45 (1984).

[5] M. I. Baskes, Phys. Rev. Lett. **59**, 2666 (1987).

[6] M. I. Baskes, J. S. Nelson, and A. F. Wright, Phys. Rev. B **40**, 6085 (1989).

[7] M. I. Baskes, Phys. Rev. B **46**, 2727 (1992).

[8] J. Lennard-Jones, Proc. R. Soc. London, Ser. A **106**, 463 (1924).

[9] J. H. Rose, J. R. Smith, F. Guinea, and J. Ferrante, Phys. Rev. B **29**, 2963 (1984).

[10] R. Laskowski, Phys. Status Solidi B **222**, 457 (2000).

[11] S. M. Foiles, M. I. Baskes, and M. S. Daw, Phys. Rev. B **33**, 7983 (1986).

[12] Y. Mishin, M. J. Mehl, D. A. Papaconstantopoulos, A. F. Voter, and J. D. Kress, Phys. Rev. B **63**, 224106 (2001).

[13] M. S. Daw, Phys. Rev. B **39**, 7441 (1989).

[14] M. I. Baskes, Mater. Chem. Phys. **50**, 152 (1997).

[15] M. I. Baskes, M. Asta, and S. G. Srinivasan, Philos. Mag. A **81**, 991 (2001).

[16] G. Kresse and J. Hafner, Phys. Rev. B **47**, 558 (1993).

[17] J. P. Perdew, in *Electronic Structure of Solids '91*, edited by P. Ziesche and H. Eschrig (Akademie, Berlin, 1991), p. 11.

[18] P. E. Blochl, Phys. Rev. B **50**, 17953 (1994).

[19] G. Kresse and J. Furthmuller, Phys. Rev. B **54**, 11169 (1996).

[20] S. M. Valone and V. Kapila, in *Shock Compression of Condensed Matter—2005*, edited by M. D. Furnish *et al.*, AIP Conf. Proc. No. 845 (AIP, Melville, NY, 2006), p. 425.

[21] L. Pauling, *The Nature of the Chemical Bond* (Cornell University Press, Ithaca, NY, 1960).

[22] J. A. Zimmerman, H. J. Gao, and F. F. Abraham, Modell. Simul. Mater. Sci. Eng. **8**, 103 (2000).

[23] W. R. Tyson and W. A. Miller, Surf. Sci. **62**, 267 (1977).

[24] R. W. Balluffi, J. Nucl. Mater. **69–70**, 240 (1978).

[25] *Vacancies and Interstitials in Metals*, edited by A. Seeger, D. Schumacher, W. Schilling, and J. Diehl (North-Holland, Amsterdam, 1970).

[26] P. Ehrhart, J. Nucl. Mater. **69–70**, 200 (1978).

[27] *Properties and Interaction of Atomic Defects in Metals and Alloys* edited by H. Ullmaier (Springer, Berlin, 1991).

[28] *Smithells Metals Reference Book* edited by E. A. Brandes (Butterworths, London, 1983).

[29] S. Japel, B. Schwager, R. Boehler, and M. Ross, Phys. Rev. Lett. **95**, 167801 (2005).

[30] V. Paidar, L. G. Wang, M. Sob, and V. Vitek, Modell. Simul. Mater. Sci. Eng. **7**, 369 (1999).